INORGANIC CHEMISTRY FRONTIERS

RESEARCH ARTICLE

View Article Online
View Journal | View Issue

Cite this: *Inorg. Chem. Front.*, 2022, **9**, 4753

Photocatalytic CO_2 reduction on Cu single atoms incorporated in ordered macroporous TiO_2 toward tunable products†

Cong Chen,[a] Ting Wang,[a] Ke Yan,[a] Shoujie Liu,[b] Yu Zhao[c] and Benxia Li*[a]

The photocatalytic conversion of CO_2 to hydrocarbons is a fascinating strategy to defuse the growing energy and environmental dilemmas, but there are great challenges in improving photocatalytic efficiency and tuning product selectivity. Both are of equal importance to increase the yield of the desired product and clarify the photocatalytic CO_2 reduction mechanism. Herein, a Cu single-atom-incorporated three-dimensional-ordered macroporous TiO_2 ($Cu_{0.01}$/3DOM-TiO_2) photocatalyst was synthesized using a template-assisted *in situ* pyrolysis method. The Cu single atoms are uniformly anchored in a 3DOM TiO_2 matrix, which not only broadens the light absorption range but also provides specific active sites for the adsorption and transformation of CO_2 molecules. The photocatalytic CO_2 reduction reaction was conducted in gas–solid and liquid–solid systems, respectively, to explore the effects of reaction modes on the CO_2 conversion efficiency and product selectivity. The results indicate that the photocatalytic CO_2 reduction reaction in gas–solid system mainly produces methane (CH_4), with a high selectivity of 83.3% and a formation rate of 43.15 μmol g^{-1} h^{-1}. In contrast, the main product in the liquid–solid system is ethylene (C_2H_4), with a selectivity of 58.4% and a formation rate of 6.99 μmol g^{-1} h^{-1}. The $Cu_{0.01}$/3DOM-TiO_2 photocatalyst shows superior activity and selectivity in the gas–solid system while favorably producing C_2H_4 in the liquid–solid system. The possible photocatalytic mechanisms of CO_2 reduction in the two different reaction systems are discussed according to *in situ* infrared spectroscopy. This work provides some new information on promoting photocatalytic CO_2 reduction to desirable products by the rational design of photocatalysts as well as tuning the reaction conditions.

Received 29th May 2022,
Accepted 19th July 2022

DOI: 10.1039/d2qi01155g

rsc.li/frontiers-inorganic

1. Introduction

Photosynthetic organisms harness solar energy to convert CO_2 and H_2O into carbohydrates and oxygen, which achieves energy transformation in nature and maintains the carbon–oxygen balance. Enlightened by natural photosynthesis, artificial photosynthesis for CO_2 reduction with H_2O powered by solar irradiation has attracted extensive interest, which is regarded as a double-benefit approach that converts greenhouse gas to chemical fuels and valuable chemicals by harvesting solar energy.[1] However, the reactivity and product selectivity of photocatalytic CO_2 reduction are always restricted by three main obstacles: (1) the difficult adsorption of reactants on photocatalysts in heterogeneous catalytic systems, (2) the high energy requirement for C–O bond activation up to 750 kJ mol^{-1}, and (3) the various intermediates and complex pathways of the CO_2 transformation process.[2,3] Hence, the rational construction of heterogeneous photocatalysts is imperative for improving the reactivity and product selectivity of CO_2 reduction, which requires the meticulous design and masterly integration of a light-harvesting component and catalytically active sites.[4]

In recent years, single-atom (SA) catalysts have emerged as new options for the design and preparation of cost-effective and high-efficiency photocatalysts, which provide 100% active metal dispersion and thus maximize metal utilization.[5] The SA catalysts can be designed on the atomic scale by rationally embellishing the isolated specific metal-atom sites on the support materials.[6] Based on the inherent functions of light absorption and photo-generated carriers supplying the support materials, SA active sites further offer catalytic centers for promoting charge separation/transfer and reactant adsorp-

[a]*Department of Chemistry, Key Laboratory of Surface & Interface Science of Polymer Materials of Zhejiang Province, Zhejiang Sci-Tech University, Hangzhou 310018, PR China. E-mail: libx@zstu.edu.cn*
[b]*Chemistry and Chemical Engineering of Guangdong Laboratory, Shantou 515063, P. R. China*
[c]*College of Material, Chemistry and Chemical Engineering, Key Laboratory of Organosilicon Chemistry and Material Technology, Ministry of Education, Hangzhou Normal University, Hangzhou, Zhejiang 311121, PR China*
† Electronic supplementary information (ESI) available. See DOI: https://doi.org/10.1039/d2qi01155g

tion/activation.[7] Moreover, the definite active centers of SA photocatalysts enable improved understanding of the fundamental mechanism of photocatalysis, and allow us to draw more precise structure–performance correlations. Therefore, various metal cocatalysts including noble metals, transition metals and rare Earth metals, have been prepared in SA sites to increase the photocatalytic efficiency.[8–12] Among them, copper (Cu) has been identified as one of the most promising cocatalysts to convert CO_2 into various hydrocarbons owing to its optimum binding ability with CO_2 and reaction intermediates.[13–16] The individual Cu atoms immobilized on light-harvesting semiconductors can act as excellent active sites for activating CO_2 molecules and stabilizing reaction intermediates in the photocatalytic CO_2 reduction reaction.[17,18] Moreover, the introduction of highly dispersed Cu heteroatoms in light-harvesting semiconductors can broaden the light-adsorption range and enhance the photoexcited charge separation efficiency.[19] Although numerous studies have highlighted the excellent catalytic activity of Cu SAs in electrocatalytic/photocatalytic CO_2 reduction,[16,20,21] the controllable and large-scale production of heterogeneous photocatalysts with Cu SAs is still challenging. Most strategies to anchor Cu SAs on light-harvesting semiconductors are explored as post-treatment methods (*e.g.* impregnation and photodeposition), where the Cu SAs tend to aggregate into nanoparticles or leach from supports during photocatalytic reactions because of the weak combination.[22,23] Hence, the *in situ* incorporation of highly stable Cu SAs in semiconductors is desirable. Meanwhile, the morphological features of the semiconductor support are a crucial factor to create stable Cu single atoms as well as heterogeneous photocatalysts with high performance, where the support not only determines the availability and stability of Cu SA sites but also supplies photogenerated electrons for CO_2 reduction. Three-dimensional ordered macroporous (3DOM) materials with an interpenetrating porous structure and high porosity can greatly facilitate CO_2 diffusion and enhance the light utilization simultaneously.[24,25] Moreover, the large specific surface area of the 3DOM support can afford more accessible Cu SA sites for CO_2 photoreduction.[26] Although some metal-modified 3DOM TiO_2 photocatalysts have been reported, the formation of metal nanoparticles with large sizes generally results in limited photocatalysis.[27,28] Our recent study indicated that Pd single atoms could be *in situ* anchored in 3DOM CeO_2 *via* a template-assisted pyrolysis method owing to the strong metal–support interaction.[29] Inspired by this, the masterly integration of catalytically active sites (Cu SAs) and a light-harvesting semiconductor (3DOM TiO_2) is expected to achieve.

In addition, tuning the selectivity of CO_2 reduction reaction to the desired product is of great significance but remains a huge challenge.[30,31] Tan and coworkers found that the ethylene selectivity of electrocatalytic CO_2 reduction with the same catalyst could be tuned by modulating the local CO_2 concentration, where the kinetics of CO_2 reduction was substantially influenced by the modulation of CO_2 mass transport.[32] Wang *et al.* reported that the introduction of N_2 into CO_2 could control the *CO coverage on Cu–Au bimetallic catalysts and thus facilitate *CO protonation for methane formation.[33] However, the effects of reaction conditions on product selectivity of CO_2 photoreduction are rarely studied. The photocatalytic CO_2 reduction reaction is commonly conducted in either a liquid–solid or a gas–solid system. Actually, the reaction system is a non-negligible factor influencing the product selectivity of CO_2 photoreduction. Therefore, exploring the effect of reaction systems on the product selectivity of photocatalytic CO_2 reduction is as important as the development of efficient photocatalysts. In this work, a heterogeneous photocatalyst of 3DOM TiO_2 doped with Cu single atoms ($Cu_{0.01}$/3DOM-TiO_2) is controllably synthesized *via* a facile template-assisted pyrolysis method. Taking this catalyst as a research model, the photocatalytic CO_2 reduction performance is studied in gas–solid and liquid–solid reaction systems, respectively, to explore the effects of reaction modes on the catalytic activity and product selectivity. Interestingly, the $Cu_{0.01}$/3DOM-TiO_2 photocatalyst exhibits higher activity and selectivity for methane (CH_4) production in the gas–solid system, while possessing a favorable capability to convert CO_2 into ethylene (C_2H_4) in the liquid–solid system. The possible photocatalytic mechanisms of CO_2 reduction in both catalytic systems are discussed according to *in situ* diffused reflection infrared Fourier transform spectroscopy (DRIFTS) measurements.

2. Experimental

2.1. Chemicals

Titanium butoxide ($C_{16}H_{36}O_4Ti$, ≥99.0%), anhydrous cupric chloride ($CuCl_2$, 98%), styrene (>99.5%, GC), potassium persulfate ($K_2S_2O_8$, AR, 99.5%), sodium hydroxide (NaOH, 97%), acetic acid glacial (CH_3COOH, ≥99.8%), ethanol (CH_3CH_2OH, ≥99.7%), methanol (CH_3OH, 99.5%), sodium sulfate anhydrous (Na_2SO_4, 99%), potassium iodide (KI, 99%), potassium hydrogen phthalate ($C_8H_5KO_4$, 99.8%), N_2 (≥99.99%), CO_2 (≥99.99%) and argon gas (≥99.99%) were obtained commercially and used without further purification.

2.2. Synthesis of Cu/3DOM-TiO_2 photocatalysts

Firstly, the monodisperse polystyrene (PS) sub-microspheres with diameters of about 260 nm were prepared using an emulsifier-free emulsion polymerization process and assembled into the PS colloidal crystal templates (CCTs) by centrifugation.[29] The as-prepared CCTs were immersed in methanol for 30 min and then dried for a moment to remove the superfluous methanol. Subsequently, the Cu/3DOM-TiO_2 photocatalysts were prepared using a template-assisted pyrolysis method. Specifically, methanol (0.5 mL), acetic acid glacial (0.5 mL), titanium butoxide (2.72 g) and a certain amount of $CuCl_2$ were mixed by vigorous stirring for 2 h to form a homogeneous precursor solution. The pretreated CCTs were immersed in the precursor solution under vacuum treatment.

After being subjected to a vacuum for 1 h, the CCTs impregnated with precursor solution were collected, dried at room temperature, and calcined in air at 550 °C for 3 h (heating rate 1 °C min^{-1}) to obtain the Cu/3DOM-TiO_2 photocatalysts. The Cu content in the Cu/3DOM-TiO_2 photocatalysts was adjusted by changing the dosage of $CuCl_2$, and the as-synthesized photocatalyst was denoted as Cu_x/3DOM-TiO_2, where x represents the molar ratio of Cu to Ti based on the dosages of $CuCl_2$ and titanium butoxide. For example, the $Cu_{0.01}$/3DOM-TiO_2 photocatalyst was prepared by adding 10.8 mg $CuCl_2$ to the precursor solution. In addition, the other Cu_x/3DOM-TiO_2 samples (x = 0.0075, 0.0125, 0.02, 0.03, 0.04 and 0.05) were also synthesized by adding the corresponding dosage of $CuCl_2$. The actual Cu contents of $Cu_{0.0075}$/3DOM-TiO_2, $Cu_{0.01}$/3DOM-TiO_2, $Cu_{0.0125}$/3DOM-TiO_2, $Cu_{0.02}$/3DOM-TiO_2, $Cu_{0.03}$/3DOM-TiO_2, $Cu_{0.04}$/3DOM-TiO_2 and $Cu_{0.05}$/3DOM-TiO_2 were measured by atomic absorption spectroscopy (AAS) as 0.51 wt%, 0.69 wt%, 1.03 wt%, 1.33 wt%, 1.98 wt%, 2.75 wt% and 3.38 wt%, respectively.

2.3. Synthesis of control samples

Several control samples including 3DOM-TiO_2, $Cu_{0.01}$/TiO_2 and TiO_2 were prepared using a similar procedure to that for preparing the $Cu_{0.01}$/3DOM-TiO_2 photocatalyst, without adding $CuCl_2$, CCTs, $CuCl_2$ and CCTs, respectively.

2.4. Characterization

The crystalline components of photocatalysts were analyzed using a powder X-ray diffractometer (XRD, DX-2700) with Cu Kα radiation. The actual Cu contents of the Cu_x/3DOM-TiO_2 photocatalysts were measured on an atomic absorption spectrophotometer (Shimadzu AA-7000). The microstructures were observed using field emission scanning electron microscopy (FESEM, ZEISS Ultra-55) operated at 3.0 kV and transmission electron microscopy (TEM, JEOL-2010) working at 200 kV. Nitrogen adsorption/desorption isotherms were recorded on a Micromeritics ASAP 2460 apparatus at 77 K, to determine the specific surface areas and the pore size distributions of the photocatalysts. Thermogravimetric (TG) analysis was performed on a thermal gravimetric analyzer (TG209F3 Tarsus, Netzsch). Raman spectra were acquired on a Horiba Scientific LabRAM HR Evolution apparatus with a 514 nm laser as the excitation source. X-ray photoelectron spectra (XPS) were measured using a Thermo Scientific K-Alpha X-ray photoelectron spectrometer, and the binding energies were calibrated with a C 1s peak at 284.8 eV as the reference. UV–vis diffuse reflectance spectra (DRS) were taken on a Shimadzu UV-2600 spectrophotometer with $BaSO_4$ as the reference. Photoluminescence (PL) spectra were measured on a HORIBA Fluoromax-4 spectrophotometer at an excitation wavelength of 350 nm. The radical intermediates generated during photocatalytic CO_2 reduction were detected using *in situ* electron spin resonance (ESR) on a Bruker model JEOL JES-FA200 spectrometer, with 5,5-dimethyl-1-pyrroline-*N*-oxide (DMPO) as a radical-trapping reagent. The X-ray absorption of fine structures (XAFS) measurements of the Cu K-edge were conducted at the BL14W1 station at the Shanghai Synchrotron Radiation Facility (SSRF), China. The spectra were recorded in fluorescent mode using a Si (311) double-crystal monochromator and a 32-element Ge solid-state detector. The electron storage ring was operated at 3.5 GeV. Cu foil and CuO were employed as the reference samples. The XAFS data were processed using Athena and Artemis software, according to the standard procedures.

2.5. Photocatalytic CO_2 reduction tests

The photocatalytic CO_2 reduction reactions were carried out in a top-irradiated reactor with a volume of 170 mL. The simulated sunlight with a main irradiation range of 320–780 nm was provided by a Xe lamp (PLS-SXE300, Beijing Perfectlight) equipped with a specific reflector, and the optical power density irradiated on the reaction solution was 200 mW cm^{-2}. The photocatalytic CO_2 reduction reaction was conducted in gas–solid and liquid–solid systems, respectively. For the gas–solid reaction mode, the slurry prepared by dispersing 5 mg photocatalyst in 1 mL ethanol was coated on a glass plate (2 × 2 cm) and then dried at 60 °C. The glass-supported photocatalyst was placed at the bottom of the reactor, and 1 mL of deionized water was dripped beside the glass plate. After CO_2 gas was blown into the reactor and absorption equilibrium was achieved in dark, the photocatalytic CO_2 reduction reaction was started under simulated sunlight. For the liquid–solid reaction mode, the reaction suspension containing 5 mg of photocatalyst and 30 mL of water was transformed in the reactor, which was bubbled with CO_2 gas for 20 min. After the sealed reactor had been kept in dark for 30 min, the photocatalytic CO_2 reduction reaction was started under simulated sunlight from a Xe lamp. The photocatalytic reactions were conducted for 4 h to obtain the average generation rates of products. The gas products (CO, CH_4, C_2H_4) were quantitatively analyzed using a gas chromatograph (GC 9790 II, FuLi) equipped with both a thermal conductivity detector (TCD) and a flame ionization detector (FID). The liquid products were identified using ^1H nuclear magnetic resonance (NMR) spectrometry in D_2O, which was performed on a Bruker AVANCE AV 400 MHz spectrometer. For the recycling experiments, the reaction system was re-blown or re-bubbled with CO_2 gas after each reaction cycle and then irradiated for the next reaction cycle.

2.6. *In situ* DRIFTS measurement

The *in situ* diffused reflection infrared Fourier transform spectroscopy (DRIFTS) analysis was performed on a Bruker TENSOR II FTIR spectrometer equipped with a mercury–cadmium–tellurium (MCT) detector cooled with liquid nitrogen. For the gas–solid reaction mode, 30 mg of the photocatalyst was placed in the test chamber, which was then subjected to a vacuum. After the background spectrum was collected from 400 to 4000 cm^{-1}, humid CO_2 gas was introduced into the test chamber to achieve adsorption–desorption equilibrium in the dark for 30 min. Subsequently, the time-dependent DRIFTS spectra were recorded upon irradiation from the Xe lamp. For the liquid–solid reaction mode, the operations

were the same as those described above, except that a drop of deionized water was dripped beside the photocatalyst on the sample holder.

3. Results and discussion

3.1. Structures and properties of photocatalysts

The Cu_x/3DOM-TiO_2 photocatalysts were synthesized *via* a template-assisted pyrolysis method as illustrated in Fig. 1a. The monodisperse PS sub-microspheres were assembled into colloidal crystal templates which were impregnated with the precursor solution containing Cu^{2+} ions and titanium butoxide. The Cu_x/3DOM-TiO_2 photocatalysts with different Cu contents were obtained *via* calcination of the colloidal crystal templates loaded with precursors in air at 550 °C for 3 h. The thermogravimetric (TG) analysis (Fig. S1, ESI†) indicated that the PS-sphere template decomposes at 400 °C in air and the precursors are completely converted into the final material below 500 °C. Therefore, it is reasonable to conduct the calcination at 550 °C for 3 h, during which the individual Cu single atoms are *in situ* anchored in the 3DOM-TiO_2 matrix. The XRD patterns of the typical $Cu_{0.01}$/3DOM-TiO_2 photocatalyst and the control samples (3DOM-TiO_2, $Cu_{0.01}$/TiO_2 and TiO_2) are shown in Fig. 1b. The photocatalysts obtained from the template-assisted synthesis ($Cu_{0.01}$/3DOM-TiO_2 and 3DOM-TiO_2) consist of anatase TiO_2 (JCPDS no. 01-562) accompanied by a small quantity of rutile TiO_2 (JCPDS no. 01-1292), while the $Cu_{0.01}$/TiO_2 and TiO_2 samples synthesized by the direct pyrolysis of precursors without the PS template present only the diffraction peaks of anatase TiO_2. The mass fractions of rutile TiO_2 (W_{Rutile}) in $Cu_{0.01}$/3DOM-TiO_2 and 3DOM-TiO_2 are estimated to be 13.86 wt% and 13.80 wt%, respectively, according to the previously reported formula:[34,35] $W_{Rutile} = A_{Rutile}/(0.884\ A_{Anatase} + A_{Rutile})$, where $A_{Anatase}$ and A_{Rutile} are the integrated intensities of the anatase (101) and rutile (110) XRD peaks. The previous study demonstrated that the calcination process assisted by a PS colloidal crystal template could produce mixed phases of anatase and rutile.[27] As a light-harvesting material, TiO_2 containing both anatase and rutile phases is desirable because the anatase/rutile junction facilitates spatial charge separation, allowing more photogenerated charge carriers to migrate to the surface and participate in redox reactions.[36] The diffraction peaks of Cu species are not observed in the XRD patterns of both the $Cu_{0.01}$/3DOM-TiO_2 and the $Cu_{0.01}$/TiO_2 samples due to the high dispersity and/or low content of Cu. Compared with TiO_2 and 3DOM-TiO_2, the typical diffraction peaks of $Cu_{0.01}$/3DOM-TiO_2 and $Cu_{0.01}$/TiO_2 present obvious shifts to lower 2θ positions (Fig. S2, ESI†), which are caused by the doping of Cu cations with larger ionic radii (Cu^{2+}, 0.73 Å; Cu^{+}, 0.77 Å; and Ti^{4+}, 0.61 Å) into TiO_2.[37,38] In addition, the anatase (101) diffraction peak of $Cu_{0.01}$/3DOM-TiO_2 and 3DOM-TiO_2

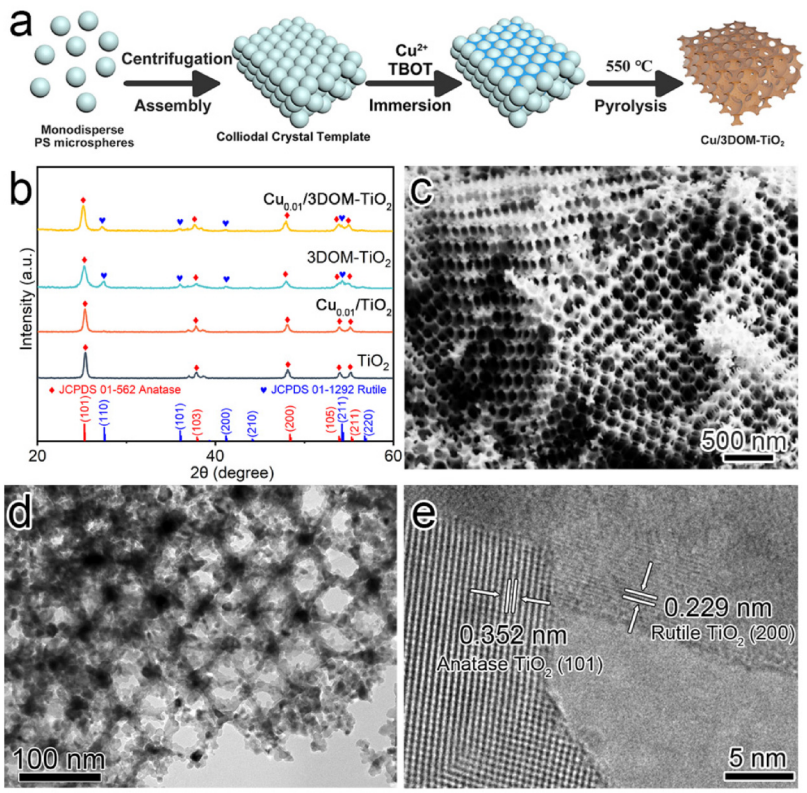

Fig. 1 (a) Schematic diagram of the synthesis of $Cu_{0.01}$/3DOM-TiO_2 photocatalyst. (b) XRD patterns of different samples; (c) SEM, (d) TEM and (e) HRTEM images of $Cu_{0.01}$/3DOM-TiO_2.

presents further shifts towards lower 2θ positions compared with those of $Cu_{0.01}/TiO_2$ and TiO_2, possibly because the special 3DOM structures result in little lattice distortion.[39,40] The SEM images (Fig. 1c; Fig. S3a, ESI†) affirm that the $Cu_{0.01}$/3DOM-TiO_2 photocatalyst exhibits a honeycomb morphology with 3D ordered macroporous structures, where the spherical voids have an average diameter of 160 nm and the walls have an average thickness of about 10 nm. These spherical voids are well arranged and interconnected. The 3DOM-TiO_2 sample (Fig. S3b, ESI†) presents a similar honeycombed morphology to that of the $Cu_{0.01}$/3DOM-TiO_2 photocatalyst. In contrast, $Cu_{0.01}/TiO_2$ (Fig. S3c, ESI†) and TiO_2 (Fig. S3d, ESI†) synthesized by the direct pyrolysis of precursors without a PS template are irregular bulks without porosity. The TEM image shown in Fig. 1d indicates that the 3DOM frameworks are constructed from numerous TiO_2 small particles. The HRTEM image (Fig. 1e) reveals the crystalline phase boundary of anatase and rutile, where the characteristic spacings of 0.352 and 0.229 nm are assignable to the (101) lattice of anatase TiO_2 and the (200) lattice of rutile TiO_2, respectively. The crystalline lattices of CuO or Cu_2O are not found in the HRTEM image of $Cu_{0.01}$/3DOM-TiO_2, suggesting that Cu element exists as highly dispersed species in this material.

The specific surface areas and pore size distributions of $Cu_{0.01}$/3DOM-TiO_2, 3DOM-TiO_2 and $Cu_{0.01}/TiO_2$ were determined using N_2 adsorption–desorption measurements (Fig. 2; Fig. S4, ESI†). Both $Cu_{0.01}$/3DOM-TiO_2 and 3DOM-TiO_2 samples display the typical type IV isotherm with a hysteresis loop, and the dominant adsorption of both samples can be identified as macropores corresponding to the step at P/P_0 = 0.8–0.995 (Fig. 2a).[41] In contrast, $Cu_{0.01}/TiO_2$ presents an extremely weak N_2 adsorption capacity (Fig. S4, ESI†) due to its large bulk morphology without porosity. $Cu_{0.01}$/3DOM-TiO_2 presents a specific surface area of 52.80 $m^2\ g^{-1}$ and a pore volume of 0.28 $cm^3\ g^{-1}$, which are higher than those of 3DOM-TiO_2 (Table S2, ESI†). The $Cu_{0.01}/TiO_2$ sample shows a very low specific surface area (3.74 $m^2\ g^{-1}$) and a negligible pore volume (0.0014 $cm^3\ g^{-1}$). The large surface area and pore volume of $Cu_{0.01}$/3DOM-TiO_2 are conducive to the sufficient exposure of active sites and the easy diffusion of CO_2 and H_2O molecules during the photocatalytic CO_2 reduction reaction.[42]

The Raman spectroscopy analysis shed light on the variations in local structures of TiO_2 in different photocatalysts. As shown in Fig. 3a, the Raman spectra of the three samples ($Cu_{0.01}$/3DOM-TiO_2, 3DOM-TiO_2 and $Cu_{0.01}/TiO_2$) exhibit five representative peaks of anatase TiO_2, which can be ascribed to the $E_{g(1)}$, $E_{g(2)}$ and $E_{g(3)}$ modes (144, 197 and 639 cm^{-1}), the B_{1g} mode (397 cm^{-1}) and the doublet of the A_{1g}/B_{1g} mode (517 cm^{-1}), respectively.[41,43] Compared with $Cu_{0.01}/TiO_2$, 3DOM-TiO_2 shows a slight shift and broadening in the characteristic A_{1g} and B_{1g} vibration peaks due to the increased structural disorder resulting from the formation of the 3DOM structure. $Cu_{0.01}$/3DOM-TiO_2 presents further broadening of the characteristic peaks because of Cu doping in 3DOM TiO_2, but no peaks of copper oxide or copper hydroxide are observed. Moreover, both 3DOM-TiO_2 and $Cu_{0.01}$/3DOM-TiO_2 show a weak peak at 448 cm^{-1} (inset in Fig. 3a), which corresponds to a characteristic vibration mode of rutile TiO_2, further confirming the coexistence of the anatase and rutile phases in the two samples.[44] The XPS technique was employed to acquire information on the surface elemental compositions and chemical states of the photocatalysts. For the three samples ($Cu_{0.01}$/3DOM-TiO_2, 3DOM-TiO_2 and $Cu_{0.01}/TiO_2$), each of the Ti 2p spectra (Fig. 3b) shows two characteristic peaks at binding energies of 458.6 and 464.3 eV, which are assignable to Ti $2p_{3/2}$ and $2p_{1/2}$ of Ti^{4+}, respectively.[45,46] Compared with $Cu_{0.01}/TiO_2$, the Ti $2p_{3/2}$ and $2p_{1/2}$ peaks of both 3DOM-TiO_2 and $Cu_{0.01}$/3DOM-TiO_2 present a 0.1 eV positive shift, which is probably caused by the lattice distortions of 3DOM-TiO_2.[47] Two peaks are deconvoluted from each O 1s spectrum (Fig. 3c), where the main peak around 529.8 eV is assigned to

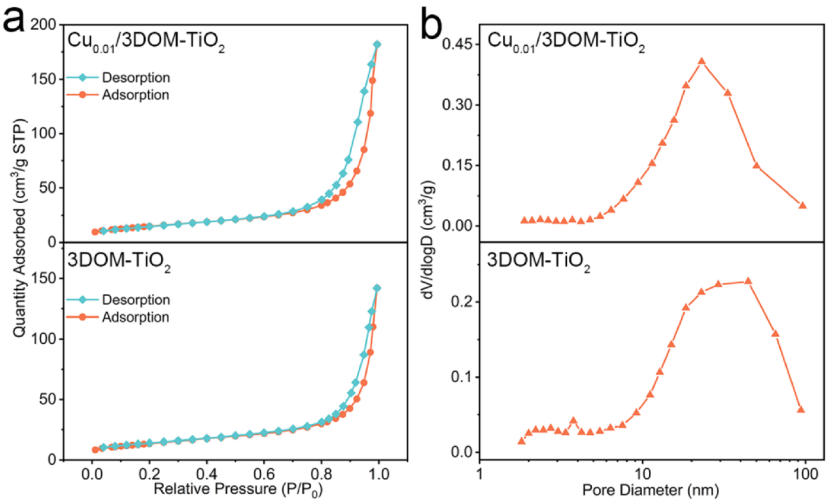

Fig. 2 (a) N_2 adsorption–desorption isotherms and (b) pore size distribution plots of $Cu_{0.01}$/3DOM-TiO_2 and 3DOM-TiO_2.

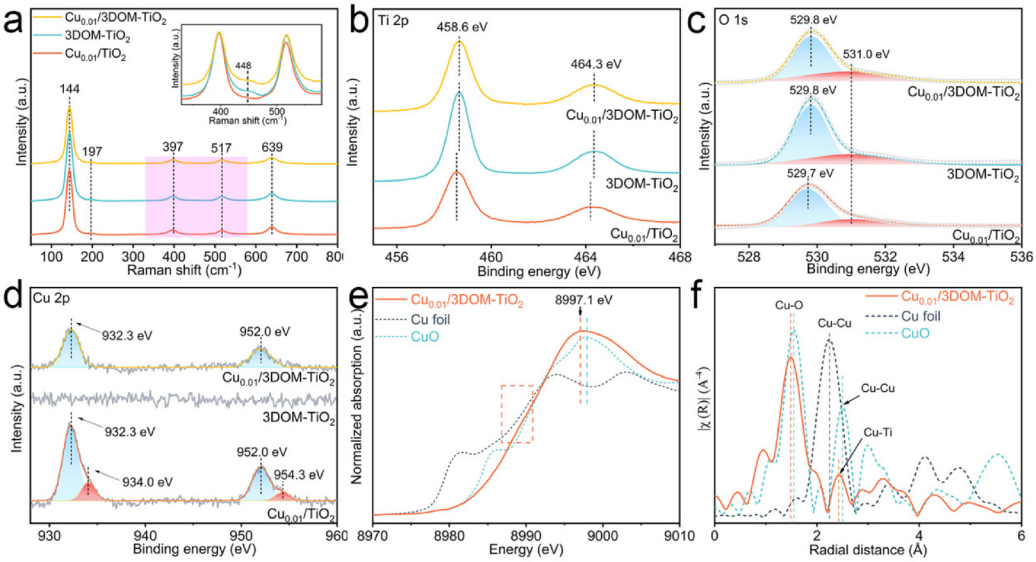

Fig. 3 (a) Raman spectra of different photocatalysts. XPS spectra of (b) Ti 2p, (c) O 1s, and (d) Cu 2p of different photocatalysts. (e) Cu K-edge XANES and (f) EXAFS spectra of $Cu_{0.01}$/3DOM-TiO_2 with the reference samples of Cu foil and CuO.

the lattice oxygen of TiO_2 and the minor peak around 531.0 eV is attributed to the surface chemisorbed oxygen on oxygen-vacancy (V_O) sites.[48–50] $Cu_{0.01}$/3DOM-TiO_2 and 3DOM-TiO_2 have higher oxygen-vacancy contents (34.63% and 30.74%) than $Cu_{0.01}/TiO_2$ (24.87%), because the high specific surface area of 3DOM-TiO_2 exposes more surface Ti sites with unsaturated coordination.[51] In Fig. 3d, two characteristic peaks centered at binding energies of 932.3 and 952.0 eV appear in the Cu 2p spectra of both $Cu_{0.01}$/3DOM-TiO_2 and $Cu_{0.01}/TiO_2$, which are approximate to the Cu $2p_{3/2}$ and $2p_{1/2}$ of Cu^+ ions,[52,53] indicating that the Cu single atoms incorporated in TiO_2 have an electronic state close to that of the Cu^+ cation. In addition, another pair of minor peaks centered at 934.0 and 954.3 eV deconvoluted from the Cu 2p spectrum of $Cu_{0.01}/TiO_2$ can be assigned to a Cu^{2+} cation with a higher oxidation state, probably due to the formation of CuO clusters.[54,55] Compared with 3DOM-TiO_2, the lack of peak shifts in the XPS spectra of $Cu_{0.01}$/3DOM-TiO_2 may be ascribable to the formation of the atomically dispersed $Cu^{\delta+}$ in the lattice of 3DOM-TiO_2 during the high-temperature calcination process as well as the low Cu content. Furthermore, the electronic structure and local coordination environment of Cu atoms in the $Cu_{0.01}$/3DOM-TiO_2 photocatalyst were studied using X-ray absorption fine structure (XAFS) analysis, in comparison with Cu foil and CuO. Fig. 3e shows the normalized Cu K-edge X-ray absorption near-edge structure (XANES) spectra, where the adsorption edge of $Cu_{0.01}$/3DOM-TiO_2 is located between those of Cu foil and CuO, indicating that the electronic state of Cu in $Cu_{0.01}$/3DOM-TiO_2 lies between those of Cu^0 and Cu^{2+}.[52] The adsorption peak of $Cu_{0.01}$/3DOM-TiO_2 is centered at 8997.1 eV and shifts a little to a lower energy compared with CuO, meaning a higher electron density of Cu single atoms in this photocatalyst than for Cu^{2+} in CuO.[56] The coordination configuration of Cu atoms in $Cu_{0.01}$/3DOM-TiO_2 is further revealed by the extended X-ray adsorption fine structure (EXAFS) spectrum (Fig. 3f). The Cu K-edge EXAFS spectrum of $Cu_{0.01}$/3DOM-TiO_2 presents two characteristic distances. The major peak centered at 1.4 Å corresponds to the direct binding of Cu atoms with lattice oxygen (Cu–O), while the minor peak located at 2.4 Å is assignable to Cu–Ti coordination in the TiO_2 environment.[57] No peak of Cu–Cu metallic binding is observed, indicating that the Cu atoms are individually doped into the lattice of TiO_2 and atomically distributed in the 3DOM-TiO_2 support.

High light-harvesting and charge separation efficiencies are fundamental requirements for efficient photocatalysis. The photoabsorption properties of bulk TiO_2, 3DOM-TiO_2, $Cu_{0.01}/TiO_2$ and $Cu_{0.01}$/3DOM-TiO_2 were measured using UV–vis diffuse reflectance spectroscopy (UV–vis DRS), as shown in Fig. 4a. The bulk TiO_2 shows absorption only in the ultraviolet region (λ < 400 nm) corresponding to the intrinsic transition from valence band (VB) to conduction band (CB). 3DOM-TiO_2 exhibits a great enhancement in its ultraviolet-harvesting ability owing to the unique 3DOM structure as well as additional absorption from 400 nm to longer wavelengths due to the formation of more oxygen vacancies.[58] With the introduction of Cu atoms, the photoabsorption above 400 nm becomes more conspicuous, suggesting the presence of more V_O defect states in TiO_2.[19] Moreover, the Cu-incorporated TiO_2 samples ($Cu_{0.01}/TiO_2$ and $Cu_{0.01}$/3DOM-TiO_2) exhibit a near-infrared absorption band near 800 nm, corresponding to d–d transitions of the dopant Cu cations.[59] For $Cu_{0.01}/TiO_2$, the photoabsorption decreases in the ultraviolet region while increasing greatly in the visible region, which is attributable to the formation of CuO on TiO_2. Photographs of the different photocatalysts are provided in Fig. 4a and Fig. S12 (ESI†), respectively. Typically, the $Cu_{0.01}$/3DOM-TiO_2 photocatalyst is

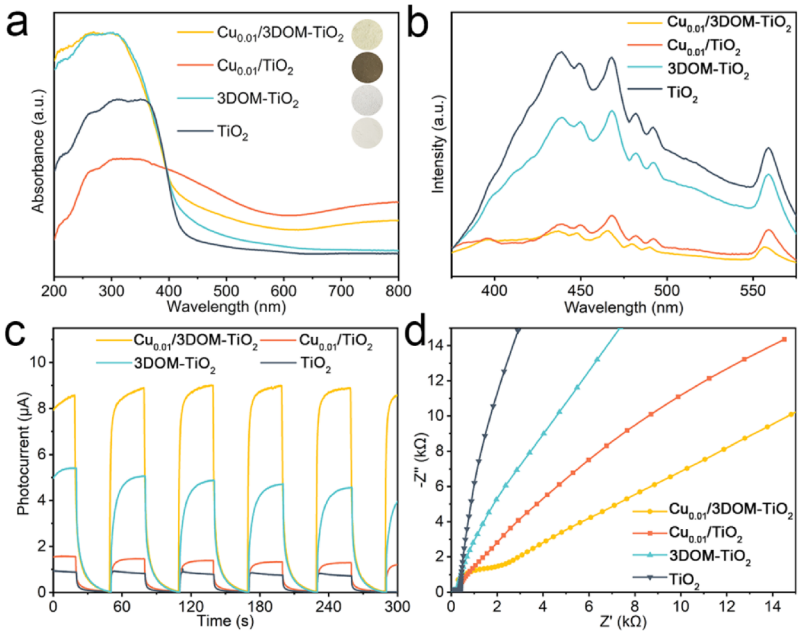

Fig. 4 (a) Kubelka–Munk transformed UV–vis absorption spectra, (b) photoluminescence spectra, (c) transient photocurrent responses, (d) electrochemical impedance spectra of different photocatalysts.

light yellow while the $Cu_{0.01}/TiO_2$ sample is dark green. The color of the Cu_x/3DOM-TiO_2 photocatalysts changes from light yellow to brown as the Cu content increases gradually (Fig. S12, ESI†). Photoluminescence (PL) spectroscopy is employed to evaluate the separation efficiency of the photogenerated electron–hole pairs under excitation of 300 nm. The $Cu_{0.01}$/3DOM-TiO_2 photocatalyst exhibits the weakest PL emission (Fig. 4b), suggesting the most efficient separation of photogenerated charge carriers.[60] The photocurrent responses and electrochemical impedance spectra (EIS) of photocatalysts were measured to further verify their photoexcited charge separation and transfer efficiencies. As shown in Fig. 4c, $Cu_{0.01}$/3DOM-TiO_2 shows the highest photocurrent response with a light on/off mode, reflecting the most efficient separation and transfer of photoexcited charge carriers. The EIS Nyquist plot of $Cu_{0.01}$/3DOM-TiO_2 presents the smallest arc radius (Fig. 4d), corresponding to the fastest charge transfer. These results demonstrate that the incorporation of Cu single atoms into 3DOM-TiO_2 affords outstanding superiority in enhancing light absorption and photogenerated charge separation/transfer efficiency. The highly dispersed Cu single-atom incorporation in TiO_2 enables efficient electron transfer *via* the Cu^+–Cu^{2+} shift.[22] The unique structure and properties of $Cu_{0.01}$/3DOM-TiO_2 make it a fascinating photocatalyst for CO_2 conversion.

3.2. Photocatalytic CO_2 reduction performance

Two typical heterogeneous photocatalytic reaction systems of gas–solid and liquid–solid modes were employed to evaluate the performance of the $Cu_{0.01}$/3DOM-TiO_2 photocatalyst toward CO_2 reduction with water under simulated sunlight. The effect of the Cu content in $Cu_{0.01}$/3DOM-TiO_2 on the photocatalysis was probed, as shown in Fig. S5,† and a volcano relationship was obtained for the photocatalytic CO_2 reduction performance relative to the Cu content. The $Cu_{0.01}$/3DOM-TiO_2 photocatalyst with a Cu/Ti molar ratio of 1% exhibited optimal performance in both reaction systems. Interestingly, the main product of the photocatalytic CO_2 reduction reaction in the gas–solid system was CH_4, while that in the liquid–solid system was C_2H_4 (Fig. S6, ESI†). Fig. 5a shows the time-dependent evolution of CH_4 and CO over the $Cu_{0.01}$/3DOM-TiO_2 photocatalyst in the gas–solid catalytic system, without H_2 evolution. As a main product, CH_4 was generated predominately from CO_2 reduction in the gas–solid catalytic reaction, with a remarkable production rate of 43.15 μmol g_{cat}^{-1} h^{-1} and a high selectivity of 83.3% (Fig. 5b). Notably, in the liquid–solid catalytic reaction, the $Cu_{0.01}$/3DOM-TiO_2 photocatalyst exhibits an excellent performance for CO_2 reduction to C_2H_4 (Fig. 5d), accompanied by the generation of CO and CH_4 by-products. The production rate of C_2H_4 reaches 6.99 μmol g_{cat}^{-1} h^{-1}, with a selectivity of 58.4%, which is of great significance due to the crucial role of C_2H_4 in the chemical industry. No liquid product is detected in the reaction solution after 4 h of irradiation (Fig. S7, ESI†). In comparison, the $Cu_{0.01}$/3DOM-TiO_2 photocatalyst presents a higher activity and product selectivity for CO_2 reduction in the gas–solid catalytic reaction while producing more valuable C_2H_4 in the liquid–solid catalytic reaction. These results indicate that the photocatalytic CO_2 reduction reactions over $Cu_{0.01}$/3DOM-TiO_2 in the two catalytic systems actually follow different reaction pathways. The promotion effects of Cu doping and the 3DOM structure on CO_2 conversion are testified by the control experiments

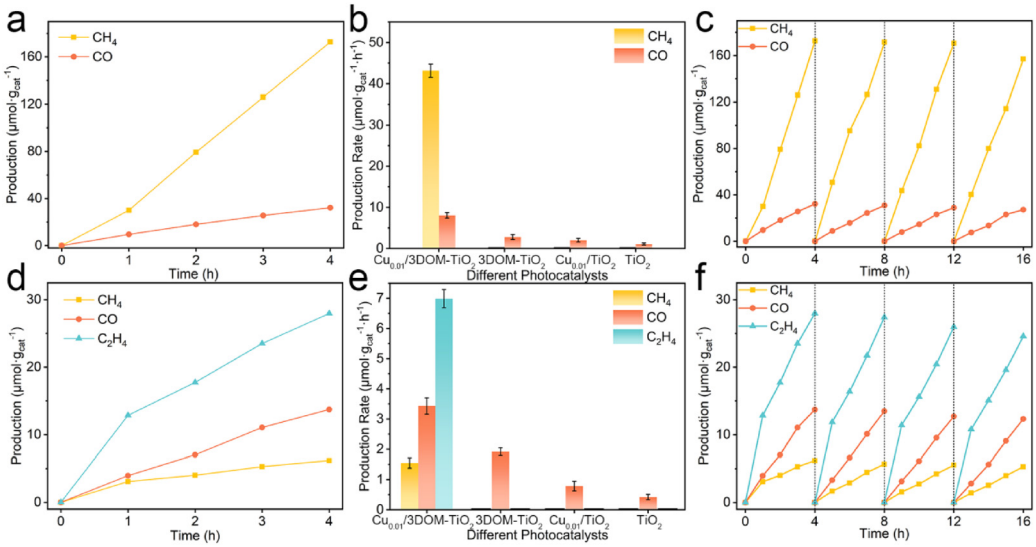

Fig. 5 Photocatalytic CO_2 reduction performance. (a–c) Gas–solid catalytic reaction: (a) product evolutions over $Cu_{0.01}$/3DOM-TiO_2, (b) generation rates of products over different photocatalysts, (c) cyclic test of $Cu_{0.01}$/3DOM-TiO_2. (d–f) Liquid–solid catalytic reaction: (d) product evolutions over $Cu_{0.01}$/3DOM-TiO_2, (e) generation rates of products over different photocatalysts, (f) cycling test of $Cu_{0.01}$/3DOM-TiO_2.

of photocatalytic reactions with 3DOM-TiO_2, $Cu_{0.01}/TiO_2$ and TiO_2, respectively. As shown in Fig. 5b and e, all the control catalysts without Cu doping or 3DOM structure present very poor photocatalysis toward CO_2 reduction in both the gas–solid and the liquid–solid systems, and none of them has the ability to convert CO_2 into CH_4 or C_2H_4, affirming that both Cu single-atom incorporation and the 3DOM structure are crucial for enhancing the photocatalytic CO_2 reduction performance. Subsequently, the durability of the $Cu_{0.01}$/3DOM-TiO_2 photocatalyst was examined by four cycles of the photocatalytic CO_2 reduction reaction with 4 h of irradiation for each cycle in the gas–solid and liquid–solid reaction systems (Fig. 5c and f), respectively. After each cycle, the photocatalyst was exposed to air for recovery. Both the excellent activity and the high selectivity were well maintained after four cycles of the photocatalytic reaction, indicating the good durability of the $Cu_{0.01}$/3DOM-TiO_2 photocatalyst. The XPS analyses (Fig. S8, ESI†) indicate that the surface composition of the $Cu_{0.01}$/3DOM-TiO_2 catalyst remains unchanged after the long-term photocatalytic CO_2 reduction reaction in both the gas–solid and liquid–solid systems, affirming the good stability of the photocatalyst. In addition, several control experiments of the photocatalytic CO_2 reduction reaction were carried out to provide evidence of the CO_2 conversion in both catalytic reaction systems. As shown in Fig. S9 (ESI†), the products are barely generated in the reaction system without CO_2, light or catalyst, indicating that all the products originate from the photocatalytic CO_2 reduction reaction. When CO_2 is replaced by N_2 in the reaction systems, small amounts of CO and CH_4 are produced at negligible rates over the $Cu_{0.01}$/3DOM-TiO_2 photocatalyst (Fig. S9b and S9d, ESI†), and the production stops after 2 h of irradiation. The slight production of CO and CH_4 can be ascribed to the reduction of surface-adsorbed CO_2 on the photocatalyst by air.

3.3. Photocatalytic reaction mechanism

The photoinduced charge transfer from the catalyst to the reactant molecules is critical for photocatalytic reactions. To probe the interfacial charge kinetics, the photocurrent responses of photocatalysts were measured in different atmospheres. The transient photocurrent recorded under an Ar atmosphere is assignable to the electron transfer from catalyst to electrode. Notably, the photocurrent measured in the CO_2-saturated electrolyte is lower than that measured in the Ar-saturated electrolyte for each photocatalyst (Fig. 6a and b), which is caused by the competitive interfacial electron transfer from the photocatalyst to the surface-adsorbed CO_2 molecules.[61] In comparison, the photocurrents of the Cu-incorporated photocatalysts ($Cu_{0.01}$/3DOM-TiO_2 and $Cu_{0.01}/TiO_2$) decline more than those of the photocatalysts without Cu (3DOM-TiO_2 and TiO_2), indicating that the incorporation of Cu is greatly beneficial to the electron transfer from the photocatalyst to the CO_2 molecules. In particular, the $Cu_{0.01}$/3DOM-TiO_2 photocatalyst shows the greatest decrease in photocurrent measured in the CO_2-saturated electrolyte, corresponding to the most efficient electron delivery from the catalyst to the CO_2 molecules. It is understandable that the high charge separation and transfer efficiencies as well as the favorable CO_2 adsorption ability of the $Cu_{0.01}$/3DOM-TiO_2 photocatalyst jointly contributes to enhancing the electron provision to CO_2 molecules. The significantly enhanced electron transfer efficiency can accelerate the CO_2 activation and the subsequent proton-coupled electron transfer process for hydrocarbon generation.[62] Furthermore, *in situ* ESR detection reveals the generation of radical intermediates during photocatalytic CO_2 reduction with water over the $Cu_{0.01}$/3DOM-TiO_2 catalyst (Fig. 6c). After 10 min of irradiation, the characteristic signal of the carbon-centered radical is obviously

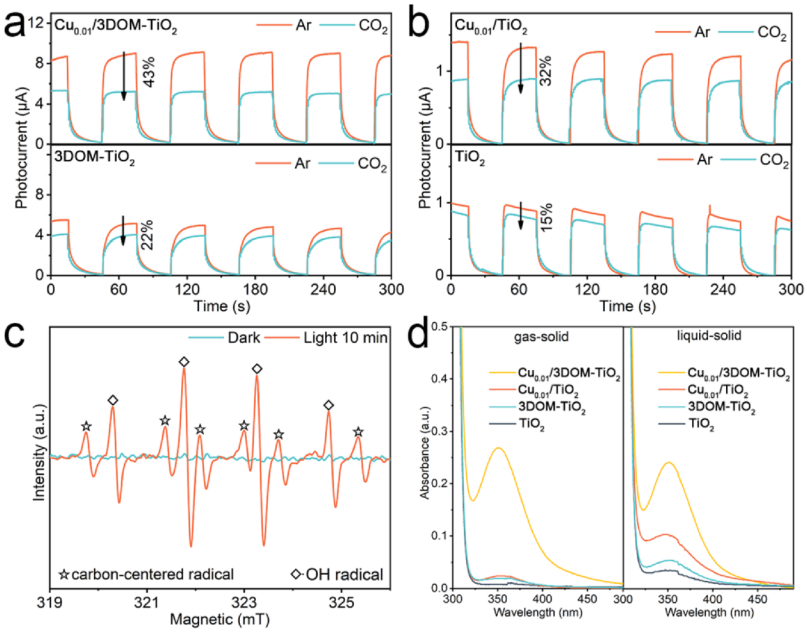

Fig. 6 (a, b) Transient photocurrents of different catalysts measured in the Ar or CO_2 saturated electrolyte, (c) *in situ* ESR detection of the photocatalytic CO_2 reduction system with $Cu_{0.01}/3DOM\text{-}TiO_2$, (d) UV–vis absorption spectra of the iodometry solution of photocatalytic CO_2 reduction over different photocatalysts in gas–solid and liquid–solid systems.

detected, affirming the activation of chemisorbed CO_2 on the photocatalyst.[63] Meanwhile, the characteristic signal of the hydroxyl radical ($^{\bullet}OH$) is also observed in the photocatalytic reaction system, which should stem from the oxidation of surface-adsorbed H_2O molecules by consuming photogenerated holes (h^+).[64] Accordingly, hydrogen peroxide (H_2O_2) as the product of the oxidation half reaction in both the photocatalytic CO_2 reduction systems is determined by iodometry (Fig. 6d).[65] The H_2O_2 production rates in gas–solid and liquid–solid reaction systems of the $Cu_{0.01}/3DOM\text{-}TiO_2$ photocatalyst are 16.85 and 15.12 μmol g_{cat}^{-1} h^{-1}, respectively, which are much higher than those of other photocatalysts (Fig. S10, ESI†). The results demonstrate that H_2O_2 has been produced from the oxidation of surface-adsorbed H_2O by the photogenerated holes and also confirm the superior activity of the $Cu_{0.01}/3DOM\text{-}TiO_2$ photocatalyst toward CO_2 reduction with water.

In situ DRIFTS spectra collected from the photocatalytic reaction systems are helpful to identify the surface-bound intermediates of CO_2 transformation and provide crucial clues for understanding the reaction pathway. *In situ* DRIFTS measurements were carried out for both the gas–solid and the liquid–solid catalytic reaction systems under Xe lamp irradiation. In both cases, four broad absorption bands appear in the 3750–3550 cm^{-1} region (Fig. S11, ESI†). The bands centered at 3727 and 3707 cm^{-1} are attributable to the stretching vibrations of surface-adsorbed –OH groups on Ti^{4+} and Ti^{3+}, respectively.[66] The bands peaking at 3626 and 3600 cm^{-1} correspond to the stretching vibrations of O–H in HCO_3^- and H_2O, respectively.[67] In comparison, the intensities of the four absorption bands in the liquid–solid catalytic system are much higher than those of the gas–solid catalytic system due to the water-rich environment of the former. The infrared adsorption signals of the CO_2-reduction intermediates are displayed in Fig. 7. The peak at 1542 cm^{-1} in the gas–solid catalytic system is attributable to the surface-bound monodentate carbonate (m-CO_3^{2-}), which is located at 1536 cm^{-1} for the liquid–solid catalytic system.[68,69] Some infrared adsorption peaks associated with the CO_2 transformation intermediates are obviously detected in both photocatalytic systems. The broad peak at 1448 cm^{-1} (Fig. 7a) or 1444 cm^{-1} (Fig. 7b) is ascribed to *COOH, a typical one-electron-reduction intermediate.[70] The emergence of the peaks at 1346 and 1559 cm^{-1} (1350 and 1548 cm^{-1}) is indicative of the formation of *HCOOH *via* the protonation process of *COOH.[18] The adsorption bands in the region of 1614–1774 cm^{-1} are assignable to *CHO, which is an intermediate generated from *HCOOH.[18,71,72] Notably, the infrared signals of the gas–solid catalytic system (Fig. 7a) are much stronger than those of the liquid–solid system (Fig. 7b), due to the higher conversion rate of the former. The low solubility of CO_2 in water restricts the reaction rate of the photocatalytic CO_2 reduction in the liquid–solid system. In addition, several distinctive signals are observed in the *in situ* DRIFTS of both catalytic systems, which provide crucial evidence to reveal the differences in the photocatalytic CO_2 reduction pathways. For the gas–solid catalytic system (Fig. 7a), the sharp peak at 1455 cm^{-1} appearing after prolonged irradiation is attributed to the *CH_3 group originating from *CHO protonation,[38,73] which is generally considered as a key intermediate for CH_4 production. For the liquid–solid catalytic system (Fig. 7b), the characteristic peak of *CH_3 is absent, but a new peak at

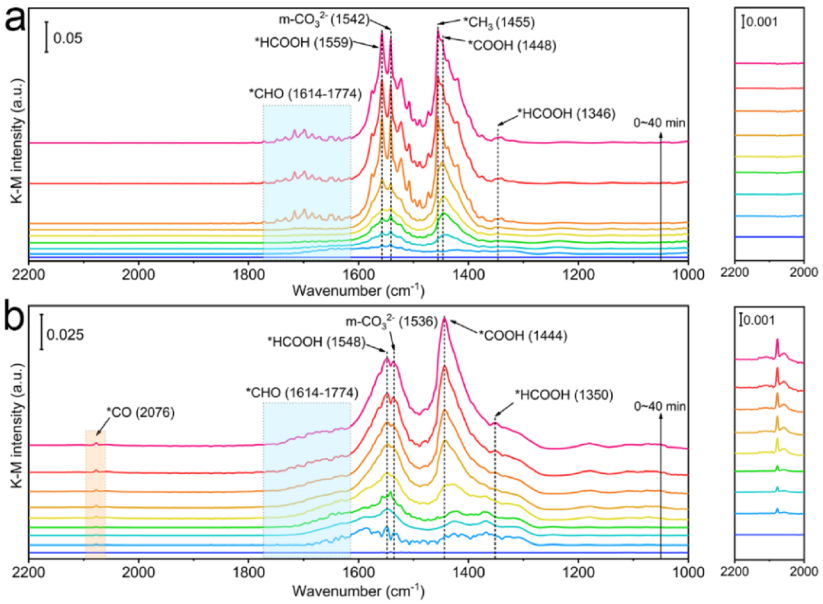

Fig. 7 *In situ* DRIFTS of the photocatalytic CO_2 reduction with $Cu_{0.01}$/3DOM-TiO_2 catalyst in two different reaction systems: (a) gas–solid catalytic system, (b) liquid–solid catalytic system.

2076 cm^{-1} is increasingly apparent with the irradiation, which can be assigned to the chemisorbed *CO.[70,74] The previous report proved that the intermolecular interaction between surface-adsorbed CO and interfacial water is critical for the formation of ethylene during the electrochemical reduction of CO.[75] The interfacial water is helpful to stabilize the CO dimer, a key intermediate in ethylene formation, by hydrogen bonding to the terminal oxygens of the adsorbed CO molecules. The porous structure of the $Cu_{0.01}$/3DOM-TiO_2 photocatalyst provides a water-rich local environment during CO_2 reduction in the liquid–solid system, which is beneficial to the stabilization and dimerization of the *CO intermediate.[76]

According to the above analyses, the photocatalytic mechanism and possible CO_2 reduction pathways over the $Cu_{0.01}$/3DOM-TiO_2 photocatalyst in two different systems are illustrated in Fig. 8. 3DOM-TiO_2 is excited to generate electron–hole pairs under simulated sunlight, and the photogenerated electrons are efficiently captured by the positively charged $Cu^{\delta+}$

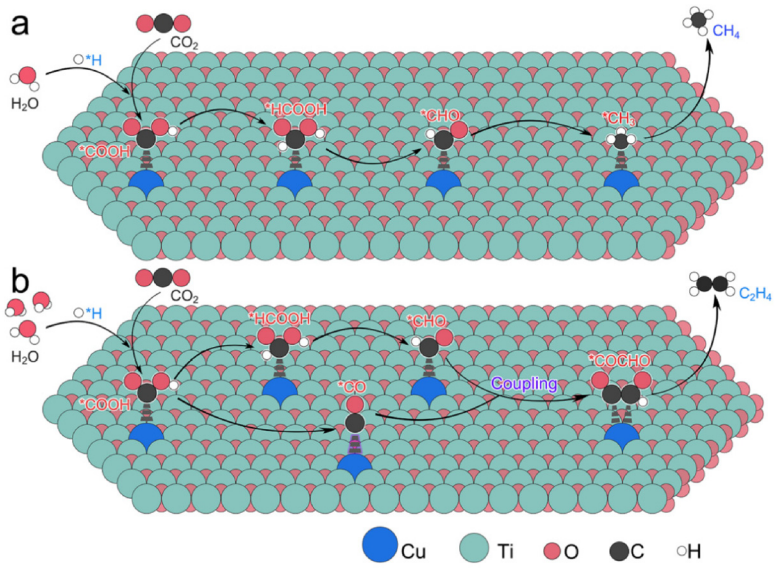

Fig. 8 The possible mechanisms of photocatalytic CO_2 reduction over $Cu_{0.01}$/3DOM-TiO_2 catalyst in two different reaction systems: (a) gas–solid catalytic system, (b) liquid–solid catalytic system.

($0 < \delta \leq 2$) single-atom sites. The enhanced electron density at Cu sites facilitates the conversion of CO_2 into hydrocarbons (CH_4 or C_2H_4) *via* the multi-proton coupled multi-electron reduction process. Specifically, the adsorption and activation of CO_2 molecules are achieved at the $Cu^{\delta+}$ active sites of photocatalyst, where the adsorbed CO_2 undergoes a continuous hydrogenation process to form *COOH, followed by the generation of *HCOOH and *CHO intermediates. In the gas–solid photocatalytic system (Fig. 8a), CH_4 is produced as the main product *via* the hydrogenation process of *CHO. On the other hand, it is widely accepted that the generation of the C_2 product undergoes three different reaction paths: (1) a *COCO intermediate from *CO dimerization, (2) a *COCHO intermediate from the dimerization between *CO and *CHO, and (3) a *CHOCHO intermediate from *CHO dimerization.[71,77,78] In the liquid–solid system of photocatalytic CO_2 reduction (Fig. 8b), the coexistence of *CO and *CHO intermediates is a crucial clue to speculate that the formation of C_2H_4 follows the pathway of the *COCHO intermediate from dimerization between *CO and *CHO. Therefore, the possible reaction pathways of photocatalytic CO_2 reduction in the present gas–solid and liquid–solid systems are described in eqn (1)–(5) and (6)–(11), respectively, where * denotes the catalytically active sites on the photocatalyst and ↑ represents the release of the gas product.

$$* + CO_2 + e^- + H^+ \rightarrow *COOH \quad (1)$$

$$*COOH + e^- + H^+ \rightarrow *HCOOH \quad (2)$$

$$*HCOOH + e^- + H^+ \rightarrow *CHO + H_2O \quad (3)$$

$$*CHO + 4e^- + 4H^+ \rightarrow *CH_3 + H_2O \quad (4)$$

$$*CH_3 + e^- + H^+ \rightarrow CH_4 \uparrow \quad (5)$$

$$* + CO_2 + e^- + H^+ \rightarrow *COOH \quad (6)$$

$$*COOH + e^- + H^+ \rightarrow *CO + H_2O \quad (7)$$

$$*COOH + e^- + H^+ \rightarrow *HCOOH \quad (8)$$

$$*HCOOH + e^- + H^+ \rightarrow *CHO + H_2O \quad (9)$$

$$*CHO + *CO \rightarrow *CO\text{–}CHO \quad (10)$$

$$*CO\text{–}CHO + 7e^- + 7H^+ \rightarrow C_2H_4 \uparrow + 2H_2O \quad (11)$$

The oxidation half-reactions in both the catalytic systems are the formation of H_2O_2 *via* the consumption of photogenerated holes by water (eqn (12) and (13)).

$$*H_2O \rightarrow H^+ + *OH^- \quad (12)$$

$$2*OH^- + 2h^+ \rightarrow H_2O_2 \quad (13)$$

The photocatalytic CO_2 reduction reaction in liquid–solid system is restricted by the low solubility of CO_2 in water (33 mM at 1 atm and 25 °C) and the poor mass transfer of CO_2 in the liquid phase.[79] However, the diffusion coefficient of CO_2 in the gas phase (~0.1 $cm^2\ s^{-1}$) is about 10 000 times that in the liquid phase (~1×10^{-5} $cm^2\ s^{-1}$), which allows the rapid delivery of CO_2 molecules to the surface of photocatalysts with uncovered active sites. The adsorption and activation of CO_2 and H_2O can be implemented more efficiently in the gas–solid system, and thus the photocatalyst shows higher activity.

4. Conclusion

In summary, the Cu single atom-incorporated 3DOM-TiO_2 photocatalyst was synthesized using a low-cost and mass-production template-assisted pyrolysis strategy and further demonstrated for solar-powered CO_2 conversion into hydrocarbons. The 3DOM structure with large surface area maximizes the exposed sites for anchoring Cu single atoms in a TiO_2 matrix, which enhances the light absorption as well as affording more accessible active sites for CO_2 reduction. The photocatalytic CO_2 reduction with H_2O was conducted in the gas–solid and liquid–solid systems, respectively, to explore the effects of reaction modes on CO_2 conversion efficiency and product selectivity. The $Cu_{0.01}$/3DOM-TiO_2 photocatalyst exhibits higher activity and selectivity for CH_4 production from CO_2 reduction in the gas–solid system while showing a favorable performance for converting CO_2 to C_2H_4 in the liquid–solid system. Both the excellent activity and the selectivity are well maintained after a long irradiation time, indicating the good durability of the $Cu_{0.01}$/3DOM-TiO_2 photocatalyst. Compared with the 3DOM-TiO_2-based photocatalysts reported previously (Table S8, ESI†), the $Cu_{0.01}$/3DOM-TiO_2 catalyst exhibits superior photocatalytic CO_2 reduction performance without using any noble metal cocatalysts. The photocatalytic mechanisms in both reaction systems were investigated by *in situ* DRIFTS analyses. It is proposed that CH_4 is generated as the main product *via* the *CHO intermediate in the gas–solid system while C_2H_4 is produced *via* the dimerization of *CO and *CHO in the liquid–solid system. This work develops a scalable strategy for preparing Cu-SA-incorporated photocatalysts but also offers a new idea for regulating the product selectivity of CO_2 photoreduction by altering the reaction system.

Author contributions

Cong Chen: methodology, investigation, data curation, visualization, writing – original draft. Ting Wang: methodology, investigation, validation. Ke Yan: investigation, validation. Shoujie Liu: software, data curation. Yu Zhao: software, funding acquisition. Benxia Li: supervision, conceptualization, writing – review & editing, funding acquisition.

Conflicts of interest

The authors declare no conflict of interest.

Acknowledgements

This work was supported by the National Natural Science Foundation of China (21471004), the Open Research Fund Program of Key Laboratory of Surface & Interface Science of Polymer Materials of Zhejiang Province (SISPM-2021-02) and the Science Foundation of Zhejiang Sci-Tech University (17062002-Y).

Notes and references

1 X. B. Li, Z. K. Xin, S. G. Xia, X. Y. Gao, C. H. Tung and L. Z. Wu, Semiconductor nanocrystals for small molecule activation via artificial photosynthesis, *Chem. Soc. Rev.*, 2020, **49**, 9028–9056.

2 C. Gao and Y. Xiong, Solar-driven artificial carbon cycle, *Chin. J. Chem.*, 2021, **40**, 153–159.

3 E. Gong, S. Ali, C. B. Hiragond, H. S. Kim, N. S. Powar, D. Kim, H. Kim and S.-I. In, Solar fuels: Research and development strategies to accelerate photocatalytic CO_2 conversion into hydrocarbon fuels, *Energy Environ. Sci.*, 2022, **15**, 880–937.

4 T. Kong, J. Low and Y. Xiong, Catalyst: how material chemistry enables solar-driven CO_2 conversion, *Chem*, 2020, **6**, 1035–1038.

5 Z.-H. Xue, D. Luan, H. Zhang and X. W. Lou, Single-atom catalysts for photocatalytic energy conversion, *Joule*, 2022, **6**, 92–133.

6 S. Shin, R. Haaring, J. So, Y. Choi and H. Lee, Highly durable heterogeneous atomic catalysts, *Acc. Chem. Res.*, 2022, **55**, 1372–1382.

7 L. Zeng and C. Xue, Single metal atom decorated photocatalysts: Progress and challenges, *Nano Res.*, 2020, **14**, 934–944.

8 J. Wei, F. L. Meng, T. Li, T. Zhang, S. Xi, W. L. Ong, X. Q. Wang, X. Zhang, M. Bosman and G. W. Ho, Spontaneous atomic sites formation in wurtzite CoO nanorods for robust CO_2 photoreduction, *Adv. Funct. Mater.*, 2021, **32**, 2109693.

9 X. Xiong, C. Mao, Z. Yang, Q. Zhang, G. I. N. Waterhouse, L. Gu and T. Zhang, Photocatalytic CO_2 reduction to CO over Ni single atoms supported on defect-rich zirconia, *Adv. Energy Mater.*, 2020, **10**, 2002928.

10 Z. Chen, S. Wu, J. Ma, S. Mine, T. Toyao, M. Matsuoka, L. Wang and J. Zhang, Non-oxidative coupling of methane: N-type doping of niobium single atoms in TiO_2–SiO_2 induces electron localization, *Angew. Chem., Int. Ed.*, 2021, **60**, 11901–11909.

11 L. Luo, L. Fu, H. Liu, Y. Xu, J. Xing, C.-R. Chang, D.-Y. Yang and J. Tang, Synergy of Pd atoms and oxygen vacancies on In_2O_3 for methane conversion under visible light, *Nat. Commun.*, 2022, **13**, 2930.

12 S. Ji, Y. Qu, T. Wang, Y. Chen, G. Wang, X. Li, J. Dong, Q. Chen, W. Zhang, Z. Zhang, S. Liang, R. Yu, Y. Wang, D. Wang and Y. Li, Rare-Earth single erbium atoms for enhanced photocatalytic CO_2 reduction, *Angew. Chem., Int. Ed.*, 2020, **59**, 10651–10657.

13 S. Ali, A. Razzaq, H. Kim and S.-I. In, Activity, selectivity, and stability of Earth-abundant $CuO/Cu_2O/Cu^0$-based photocatalysts toward CO_2 reduction, *Chem. Eng. J.*, 2022, **429**, 131579.

14 Z. Sun, Y. Hu, D. Zhou, M. Sun, S. Wang and W. Chen, Factors influencing the performance of copper-bearing catalysts in the CO_2 reduction system, *ACS Energy Lett.*, 2021, **6**, 3992–4022.

15 T. Yang, X. Mao, Y. Zhang, X. Wu, L. Wang, M. Chu, C.-W. Pao, S. Yang, Y. Xu and X. Huang, Coordination tailoring of Cu single sites on C_3N_4 realizes selective CO_2 hydrogenation at low temperature, *Nat. Commun.*, 2021, **12**, 6022.

16 J. Wang, T. Heil, B. Zhu, C.-W. Tung, J. Yu, H. M. Chen, M. Antonietti and S. Cao, A single Cu-center containing enzyme-mimic enabling full photosynthesis under CO_2 reduction, *ACS Nano*, 2020, **14**, 8584–8593.

17 H. X. Zhang, Q. L. Hong, J. Li, F. Wang, X. Huang, S. Chen, W. Tu, D. Yu, R. Xu, T. Zhou and J. Zhang, Isolated square-planar copper center in boron imidazolate nanocages for photocatalytic reduction of CO_2 to CO, *Angew. Chem., Int. Ed.*, 2019, **58**, 11752–11756.

18 Y. Yu, X. Dong, P. Chen, Q. Geng, H. Wang, J. Li, Y. Zhou and F. Dong, Synergistic effect of Cu single atoms and Au–Cu alloy nanoparticles on TiO_2 for efficient CO_2 photoreduction, *ACS Nano*, 2021, **15**, 14453–14464.

19 Y. Zhao, Y. Zhao, R. Shi, B. Wang, G. I. N. Waterhouse, L. Z. Wu, C. H. Tung and T. Zhang, Tuning oxygen vacancies in ultrathin TiO_2 nanosheets to boost photocatalytic nitrogen fixation up to 700 nm, *Adv. Mater.*, 2019, **31**, 1806482.

20 Q. Zhao, C. Zhang, R. Hu, Z. Du, J. Gu, Y. Cui, X. Chen, W. Xu, Z. Cheng, S. Li, B. Li, Y. Liu, W. Chen, C. Liu, J. Shang, L. Song and S. Yang, Selective etching quaternary MAX phase toward single atom copper immobilized MXene ($Ti_3C_2Cl_x$) for efficient CO_2 electroreduction to methanol, *ACS Nano*, 2021, **15**, 4927–4936.

21 H. Bao, Y. Qiu, X. Peng, J.-A. Wang, Y. Mi, S. Zhao, X. Liu, Y. Liu, R. Cao, L. Zhuo, J. Ren, J. Sun, J. Luo and X. Sun, Isolated copper single sites for high-performance electroreduction of carbon monoxide to multicarbon products, *Nat. Commun.*, 2021, **12**, 238.

22 Y. Zhang, J. Zhao, H. Wang, B. Xiao, W. Zhang, X. Zhao, T. Lv, M. Thangamuthu, J. Zhang, Y. Guo, J. Ma, L. Lin, J. Tang, R. Huang and Q. Liu, Single-atom Cu anchored catalysts for photocatalytic renewable H_2 production with a quantum efficiency of 56%, *Nat. Commun.*, 2022, **13**, 58.

23 Y. Zhang, B. Xia, J. Ran, K. Davey and S. Z. Qiao, Atomic-level reactive sites for semiconductor-based photocatalytic CO_2 reduction, *Adv. Energy Mater.*, 2020, **10**, 1903879.

24 F. Wen and W. Liu, Three-dimensional ordered macroporous materials for photocatalysis: Design and applications, *J. Mater. Chem. A*, 2021, **9**, 18129–18147.

25 A.-Y. Lo and F. Taghipour, Ordered mesoporous photocatalysts for CO_2 photoreduction, *J. Mater. Chem. A*, 2021, **9**, 26430–26453.
26 X. Z. Zheng, J. Han, Y. Fu, Y. Deng, Y. Y. Liu, Y. Yang, T. Wang and L. W. Zhang, Highly efficient CO_2 reduction on ordered porous Cu electrode derived from Cu_2O inverse opals, *Nano Energy*, 2018, **48**, 93–100.
27 J. Jiao, Y. Wei, Y. Zhao, Z. Zhao, A. Duan, J. Liu, Y. Pang, J. Li, G. Jiang and Y. Wang, AuPd/3DOM-TiO_2 catalysts for photocatalytic reduction of CO_2: High efficient separation of photogenerated charge carriers, *Appl. Catal., B*, 2017, **209**, 228–239.
28 C. Wang, X. Liu, W. He, Y. Zhao, Y. Wei, J. Xiong, J. Liu, J. Li, W. Song, X. Zhang and Z. Zhao, All-solid-state Z-scheme photocatalysts of g-C_3N_4/Pt/macroporous-(TiO_2@carbon) for selective boosting visible-light-driven conversion of CO_2 to CH_4, *J. Catal.*, 2020, **389**, 440–449.
29 X. Tao, R. Long, D. Wu, Y. Hu, G. Qiu, Z. Qi, B. Li, R. Jiang and Y. Xiong, Anchoring positively charged Pd single atoms in ordered porous ceria to boost catalytic activity and stability in suzuki coupling reactions, *Small*, 2020, **16**, 2001782.
30 H. S. Jeon, J. Timoshenko, C. Rettenmaier, A. Herzog, A. Yoon, S. W. Chee, S. Oener, U. Hejral, F. T. Haase and B. R. Cuenya, Selectivity control of Cu nanocrystals in a gas-fed flow cell through CO_2 pulsed electroreduction, *J. Am. Chem. Soc.*, 2021, **143**, 7578–7587.
31 J. Fu, K. Jiang, X. Qiu, J. Yu and M. Liu, Product selectivity of photocatalytic CO_2 reduction reactions, *Mater. Today*, 2020, **32**, 222–243.
32 Y. C. Tan, K. B. Lee, H. Song and J. Oh, Modulating local CO_2 concentration as a general strategy for enhancing C–C coupling in CO_2 electroreduction, *Joule*, 2020, **4**, 1104–1120.
33 X. Wang, P. Ou, J. Wicks, Y. Xie, Y. Wang, J. Li, J. Tam, D. Ren, J. Y. Howe, Z. Wang, A. Ozden, Y. Z. Finfrock, Y. Xu, Y. Li, A. S. Rasouli, K. Bertens, A. H. Ip, M. Graetzel, D. Sinton and E. H. Sargent, Gold-in-copper at low *CO coverage enables efficient electromethanation of CO_2, *Nat. Commun.*, 2021, **12**, 3387.
34 X. Wang, S. Shen, Z. Feng and C. Li, Time-resolved photoluminescence of anatase/rutile TiO_2 phase junction revealing charge separation dynamics, *Chin. J. Catal.*, 2016, **37**, 2059–2068.
35 Q. Xu, Y. Ma, J. Zhang, X. Wang, Z. Feng and C. Li, Enhancing hydrogen production activity and suppressing CO formation from photocatalytic biomass reforming on Pt/TiO_2 by optimizing anatase–rutile phase structure, *J. Catal.*, 2011, **278**, 329–335.
36 C. Peng, T. Zhou, P. Wei, H. Ai, B. Zhou, H. Pan, W. Xu, J. Jia, K. Zhang, H. Wang and H. Yu, Regulation of the rutile anatase TiO_2 phase junction *in situ* grown on -OH terminated $Ti_3C_2T_x$ (MXene) towards remarkably enhanced photocatalytic hydrogen evolution, *Chem. Eng. J.*, 2022, **439**, 135685.
37 B.-R. Chen, V.-H. Nguyen, J. C. S. Wu, R. Martin and K. Kočí, Production of renewable fuels by the photohydrogenation of CO_2: effect of the Cu species loaded onto TiO_2 photocatalysts, *Phys. Chem. Chem. Phys.*, 2016, **18**, 4942–4951.
38 N. Li, B. Wang, Y. Si, F. Xue, J. Zhou, Y. Lu and M. Liu, Toward high-value hydrocarbon generation by photocatalytic reduction of CO_2 in water vapor, *ACS Catal.*, 2019, **9**, 5590–5602.
39 D. Qi, L. Lu, Z. Xi, L. Wang and J. Zhang, Enhanced photocatalytic performance of TiO_2 based on synergistic effect of Ti^{3+} self-doping and slow light effect, *Appl. Catal., B*, 2014, **160–161**, 621–628.
40 M. Zhang, W. Liao, Y. Wei, C. Wang, Y. Fu, Y. Gao, L. Zhu, W. Zhu and H. Li, Aerobic oxidative desulfurization by nanoporous tungsten oxide with oxygen defects, *ACS Appl. Nano Mater.*, 2021, **4**, 1085–1093.
41 S. Wu, Z. Chen, W. Yue, S. Mine, T. Toyao, M. Matsuoka, X. Xi, L. Wang and J. Zhang, Single-atom high-valent Fe(IV) for promoted photocatalytic nitrogen hydrogenation on porous TiO_2-SiO_2, *ACS Catal.*, 2021, **11**, 4362–4371.
42 Y. Zhang, C. Cao, X.-T. Wu and Q.-L. Zhu, Three-dimensional porous copper-decorated bismuth-based nanofoam for boosting the electrochemical reduction of CO_2 to formate, *Inorg. Chem. Front.*, 2021, **8**, 2461–2467.
43 J. A. Benavides, C. P. Trudeau, L. F. Gerlein and S. G. Cloutier, Laser selective photoactivation of amorphous TiO_2 films to anatase and/or rutile crystalline phases, *ACS Appl. Energy Mater.*, 2018, **1**, 3607–3613.
44 Z. Luo, A. S. Poyraz, C.-H. Kuo, R. Miao, Y. Meng, S.-Y. Chen, T. Jiang, C. Wenos and S. L. Suib, Crystalline mixed phase (anatase/rutile) mesoporous titanium dioxides for visible light photocatalytic activity, *Chem. Mater.*, 2014, **27**, 6–17.
45 Y. Ma, X. Yi, S. Wang, T. Li, B. Tan, C. Chen, T. Majima, E. R. Waclawik, H. Zhu and J. Wang, Selective photocatalytic CO_2 reduction in aerobic environment by microporous Pd-porphyrin-based polymers coated hollow TiO_2, *Nat. Commun.*, 2022, **13**, 1400.
46 S. Jiang, K. Zhao, M. Al-Mamun, Y. L. Zhong, P. Liu, H. Yin, L. Jiang, S. Lowe, J. Qi, R. Yu, D. Wang and H. Zhao, Design of three-dimensional hierarchical TiO_2/$SrTiO_3$ heterostructures towards selective CO_2 photoreduction, *Inorg. Chem. Front.*, 2019, **6**, 1667–1674.
47 T. Wu, X. Zhu, Z. Xing, S. Mou, C. Li, Y. Qiao, Q. Liu, Y. Luo, X. Shi, Y. Zhang and X. Sun, Greatly improving electrochemical N_2 reduction over TiO_2 nanoparticles by Iron doping, *Angew. Chem., Int. Ed.*, 2019, **58**, 18449–18453.
48 J. Y. Do, R. K. Chava, K. K. Mandari, N.-K. Park, H.-J. Ryu, M. W. Seo, D. Lee, T. S. Senthil and M. Kang, Selective methane production from visible-light-driven photocatalytic carbon dioxide reduction using the surface plasmon resonance effect of superfine silver nanoparticles anchored on lithium titanium dioxide nanocubes (Ag@Li_xTiO_2), *Appl. Catal., B*, 2018, **237**, 895–910.

49 M. Xiao, L. Zhang, B. Luo, M. Lyu, Z. Wang, H. Huang, S. Wang, A. Du and L. Wang, Molten-salt-mediated synthesis of an atomic nickel Co-catalyst on TiO_2 for improved photocatalytic H_2 evolution, *Angew. Chem., Int. Ed.*, 2020, **59**, 7230–7234.

50 Z. Wang, X. Mao, P. Chen, M. Xiao, S. A. Monny, S. Wang, M. Konarova, A. Du and L. Wang, Understanding the roles of oxygen vacancies in hematite-based photoelectrochemical processes, *Angew. Chem., Int. Ed.*, 2019, **58**, 1030–1034.

51 C. Liu, Y. Qin, W. Guo, Y. Shi, Z. Wang, Y. Yu and L. Wu, Visible-light-driven photocatalysis over nano-TiO_2 with different morphologies: From morphology through active site to photocatalytic performance, *Appl. Surf. Sci.*, 2022, **580**, 152262.

52 G. Wang, C.-T. He, R. Huang, J. Mao, D. Wang and Y. Li, Photoinduction of Cu single atoms decorated on UiO-66-NH_2 for enhanced photocatalytic reduction of CO_2 to liquid fuels, *J. Am. Chem. Soc.*, 2020, **142**, 19339–19345.

53 J. Yang, X. Zhu, Z. Mo, J. Yi, J. Yan, J. Deng, Y. Xu, Y. She, J. Qian, H. Xu and H. Li, A multidimensional In_2S_3–$CuInS_2$ heterostructure for photocatalytic carbon dioxide reduction, *Inorg. Chem. Front.*, 2018, **5**, 3163–3169.

54 J. Y. Do, N. Son, R. K. Chava, K. K. Mandari, S. Pandey, V. Kumaravel, T. S. Senthil, S. W. Joo and M. Kang, Plasmon-induced hot electron amplification and effective charge separation by Au nanoparticles sandwiched between copper titanium phosphate nanosheets and improved carbon dioxide conversion to methane, *ACS Sustainable Chem. Eng.*, 2020, **8**, 18646–18660.

55 A. A. Liu, L. C. Liu, Y. Cao, J. M. Wang, R. Si, F. Gao and L. Dong, Controlling dynamic structural transformation of atomically dispersed CuO_x species and influence on their catalytic performances, *ACS Catal.*, 2019, **9**, 9840–9851.

56 Y. Wang, Z. Chen, P. Han, Y. Du, Z. Gu, X. Xu and G. Zheng, Single-atomic Cu with multiple oxygen vacancies on ceria for electrocatalytic CO_2 reduction to CH_4, *ACS Catal.*, 2018, **8**, 7113–7119.

57 B.-H. Lee, S. Park, M. Kim, A. K. Sinha, S. C. Lee, E. Jung, W. J. Chang, K.-S. Lee, J. H. Kim, S.-P. Cho, H. Kim, K. T. Nam and T. Hyeon, Reversible and cooperative photoactivation of single-atom Cu/TiO_2 photocatalysts, *Nat. Mater.*, 2019, **18**, 620–626.

58 Z. Xu, C. Guo, X. Liu, L. Li, L. Wang, H. Xu, D. Zhang, C. Li, Q. Li and W. Wang, Ag nanoparticles anchored organic/inorganic Z-Scheme 3DOMM-TiO_2-based heterojunction for efficient photocatalytic and photoelectrochemical water splitting, *Chin. J. Catal.*, 2022, **43**, 1360–1370.

59 X. Lv, D. Y. S. Yan, F. L.-Y. Lam, Y. H. Ng, S. Yin and A. K. An, Solvothermal synthesis of copper-doped BiOBr microflowers with enhanced adsorption and visible-light driven photocatalytic degradation of norfloxacin, *Chem. Eng. J.*, 2020, **401**, 126012.

60 R. K. Chava, J. Y. Do and M. Kang, Enhanced photoexcited carrier separation in CdS–SnS_2 heteronanostructures: A new 1D–0D visible-light photocatalytic system for the hydrogen evolution reaction, *J. Mater. Chem. A*, 2019, **7**, 13614–13628.

61 N. Zhang, A. Jalil, D. Wu, S. Chen, Y. Liu, C. Gao, W. Ye, Z. Qi, H. Ju, C. Wang, X. Wu, L. Song, J. Zhu and Y. Xiong, Refining defect states in $W_{18}O_{49}$ by Mo doping: A strategy for tuning N_2 activation towards solar-driven nitrogen fixation, *J. Am. Chem. Soc.*, 2018, **140**, 9434–9443.

62 X. Chang, T. Wang and J. Gong, CO_2 photo-reduction: Insights into CO_2 activation and reaction on surfaces of photocatalysts, *Energy Environ. Sci.*, 2016, **9**, 2177–2196.

63 S. Kreft, R. Schoch, J. Schneidewind, J. Rabeah, E. V. Kondratenko, V. A. Kondratenko, H. Junge, M. Bauer, S. Wohlrab and M. Beller, Improving selectivity and activity of CO_2 reduction photocatalysts with oxygen, *Chem*, 2019, **5**, 1818–1833.

64 Y. Nosaka and A. Nosaka, Understanding hydroxyl radical (•OH) generation processes in photocatalysis, *ACS Energy Lett.*, 2016, **1**, 356–359.

65 Z. Tian, C. Han, Y. Zhao, W. Dai, X. Lian, Y. Wang, Y. Zheng, Y. Shi, X. Pan, Z. Huang, H. Li and W. Chen, Efficient photocatalytic hydrogen peroxide generation coupled with selective benzylamine oxidation over defective ZrS_3 nanobelts, *Nat. Commun.*, 2021, **12**, 2039.

66 R. Long, Y. Li, Y. Liu, S. Chen, X. Zheng, C. Gao, C. He, N. Chen, Z. Qi, L. Song, J. Jiang, J. Zhu and Y. Xiong, Isolation of Cu atoms in Pd lattice: Forming highly selective sites for photocatalytic conversion of CO_2 to CH_4, *J. Am. Chem. Soc.*, 2017, **139**, 4486–4492.

67 Ș. Neațu, J. A. Maciá-Agulló, P. Concepción and H. Garcia, Gold–copper nanoalloys supported on TiO_2 as photocatalysts for CO_2 reduction by water, *J. Am. Chem. Soc.*, 2014, **136**, 15969–15976.

68 Y. Huang, K. Li, J. Zhou, J. Guan, F. Zhu, K. Wang, M. Liu, W. Chen and N. Li, Nitrogen-stabilized oxygen vacancies in TiO_2 for site-selective loading of Pt and CoO_x cocatalysts toward enhanced photoreduction of CO_2 to CH_4, *Chem. Eng. J.*, 2022, **439**, 135744.

69 W. He, Y. Wei, J. Xiong, Z. Tang, W. Song, J. Liu and Z. Zhao, Insight into reaction pathways of CO_2 photoreduction into CH_4 over hollow microsphere Bi_2MoO_6-supported Au catalysts, *Chem. Eng. J.*, 2022, **433**, 133540.

70 W. Wang, C. Deng, S. Xie, Y. Li, W. Zhang, H. Sheng, C. Chen and J. Zhao, Photocatalytic C–C coupling from carbon dioxide reduction on copper oxide with mixed-valence copper(I)/copper(II), *J. Am. Chem. Soc.*, 2021, **143**, 2984–2993.

71 W. Ma, S. Xie, T. Liu, Q. Fan, J. Ye, F. Sun, Z. Jiang, Q. Zhang, J. Cheng and Y. Wang, Electrocatalytic reduction of CO_2 to ethylene and ethanol through hydrogen-assisted C–C coupling over fluorine-modified copper, *Nat. Catal.*, 2020, **3**, 478–487.

72 B. N. Choi, J. Y. Seo, Z. An, P. J. Yoo and C.-H. Chung, An *in situ* spectroscopic study on the photochemical CO_2 reduction on $CsPbBr_3$ perovskite catalysts embedded in a porous copper scaffold, *Chem. Eng. J.*, 2022, **430**, 132807.

73 R. Zhang, H. Wang, S. Tang, C. Liu, F. Dong, H. Yue and B. Liang, Photocatalytic oxidative dehydrogenation of ethane using CO_2 as a soft oxidant over Pd/TiO_2 catalysts to C_2H_4 and syngas, *ACS Catal.*, 2018, **8**, 9280–9286.

74 M. Wang, M. Shen, X. Jin, J. Tian, M. Li, Y. Zhou, L. Zhang, Y. Li and J. Shi, Oxygen vacancy generation and stabilization in CeO_{2-x} by Cu introduction with improved CO_2 photocatalytic reduction activity, *ACS Catal.*, 2019, **9**, 4573–4581.

75 J. Li, X. Li, C. M. Gunathunge and M. M. Waegele, Hydrogen bonding steers the product selectivity of electrocatalytic CO reduction, *Proc. Natl. Acad. Sci. U. S. A.*, 2019, **116**, 9220–9229.

76 P. B. Joshi, N. Karki and A. J. Wilson, Electrocatalytic CO_2 reduction in acetonitrile enhanced by the local environment and mass transport of H_2O, *ACS Energy Lett.*, 2022, **7**, 602–609.

77 J. X. Hao, D. Yang, J. J. Wu, B. X. Ni, L. J. Wei, Q. J. Xu, Y. L. Min and H. X. Li, Utilizing new metal phase nanocomposites deep photocatalytic conversion of CO_2 to C_2H_4, *Chem. Eng. J.*, 2021, **423**, 130190.

78 L. Hou, J. Han, C. Wang, Y. Zhang, Y. Wang, Z. Bai, Y. Gu, Y. Gao and X. Yan, Ag nanoparticle embedded Cu nanoporous hybrid arrays for the selective electrocatalytic reduction of CO_2 towards ethylene, *Inorg. Chem. Front.*, 2020, **7**, 2097–2106.

79 H. Huang, R. Shi, Z. Li, J. Zhao, C. Su and T. Zhang, Triphase photocatalytic CO_2 reduction over silver-decorated titanium oxide at a gas–water boundary, *Angew. Chem.*, 2022, **61**, e202200802.